Estimation of kinetic model parameters in fluorescence optical diffusion tomography

Adam B. Milstein, Kevin J. Webb, and Charles A. Bouman

School of Electrical and Computer Engineering, Purdue University, West Lafayette, Indiana 47907-2035

Received July 30, 2004; revised manuscript received January 21, 2005; accepted January 21, 2005

We present a technique for reconstructing the spatially dependent dynamics of a fluorescent contrast agent in turbid media. The dynamic behavior is described by linear and nonlinear parameters of a compartmental model or some other model with a deterministic functional form. The method extends our previous work in fluorescence optical diffusion tomography by parametrically reconstructing the time-dependent fluorescent yield. The reconstruction uses a Bayesian framework and parametric iterative coordinate descent optimization, which is closely related to Gauss–Seidel methods. We demonstrate the method with a simulation study.

OCIS codes: 170.6280, 290.7050, 100.3010, 100.3190, 100.6950, 170.3010, 290.3200.

1. INTRODUCTION

In optical imaging of diseased tissue, the use of fluorescent agents in imaging diseased tissue has attracted considerable interest owing to the potential for high specificity and contrast.[1] Injected fluorophores may accumulate in diseased tissue as a result of the increased vascular density[2] or by means of selective targeting.[3–6] As in positron emission tomography (PET), the reconstruction of optical contrast agent kinetics can provide useful physiological information. Several groups of researchers have measured the dynamic behavior of injected optical contrast agents in animal or human subjects.[8–13] Gurfinkel *et al.*[11] used an intensified CCD camera to measure the pharmacokinetics of fluorescent agents in a canine with mammary tumors and fitted the image sequence to a biexponential decay function that arises from a compartmental model. The study employed indocyanine green (ICG), which is believed to act as a nonselective blood pool agent, and carotene-conjugated 2-devinyl-2-(1-hexyloxyethyl) pyropheophorbide (HPPH-car), a photosensitizer that is believed to accumulate selectively in diseased tissue. A model parameter related to the dye's uptake rate showed significant contrast between diseased and surrounding tissue for HPPH-car but not for ICG. Cuccia *et al.*[13] measured the dynamics of two light-absorbing dyes, ICG and methylene blue in an adenocarcinoma rat tumor model by use of an optical probe with magnetic resonance imaging coregistration. Owing to its small molecular weight of 373.9 Da, the methylene blue temporal dynamics were dominated by blood flow effects. From the methylene blue measurements, the authors observed variations in perfusion within the rat tumor. In contrast, ICG binds to albumin in the blood, with a resulting effective molecular weight of 66 kDa. Hence ICG's temporal dynamics are dominated by the movement of albumin across the capillary membrane between the plasma and the extravascular, extracellular space. Cuccia *et al.* used ICG dynamics to compute a physiologic parameter related to capillary permeability.

In optical diffusion tomography (ODT), volume images of the absorption coefficient, the scattering coefficient, or the fluorescent yield and lifetime parameters are reconstructed from several optical measurements made on the surface.[14] Fluorescence optical diffusion tomography (FODT) refers specifically to the reconstruction of the fluorescence parameters.[15] Laser or light-emitting-diode sources inject light into the tissue at the fluorophore's excitation wavelength. The light is modulated with a short pulse, modulated with an RF sinewave, or unmodulated. The fluorophore absorbs the incident light and then decays to its ground state with some characteristic time constant, emitting some of the light at a longer wavelength. The emitted photons are then measured by an array of detection devices. From the data, one can reconstruct images of the fluorescent yield (a measure of the fluorescence efficiency) and the fluorescence lifetime (the fluorescent decay parameter). Multiple photon scattering in tissue must be properly accounted for in the reconstruction.[16,17] Diffusion or radiative transport models are used to describe the propagation of light through the highly scattering domain.[18] As a result of the multiple scattering of light, FODT must be used to quantify drug concentration accurately in issue regions that are not directly under the skin surface.

Previously, the time-varying absorption coefficient was reconstructed in a cylindrical phantom[19] and in the human brain[20] by solving the inverse problem separately for each image in a time sequence. However, in some cases, the unknown image may not reasonably be considered constant over the instrument's measurement time. In addition, independent reconstruction of each image in the sequence ignores correlations in the image over time. Kolehmainen *et al.* presented a state-estimation approach to the time-varying optical diffusion tomography problem that models the unknown image as a stochastic process governed by a stochastic difference equation.[21] This method solves the inverse problem by using extended Kalman filter and Kalman smoother techniques. The au-

thors demonstrate their method with synthetic data from a two-dimensional phantom and, in a subsequent investigation, on real hemodynamic data from the human motor cortex.[22] This approach has shown promise for dynamic imaging problems where the time variation cannot be accurately parameterized by a known, deterministic model alone. However, in practical three-dimensional imaging problems, reconstructing a time sequence of images and updating large estimator covariance matrices may pose some difficulty, owing to storage and computation requirements. Other dynamic imaging approaches have been investigated, including space–time regularization operators,[23–25] principal components analysis,[26] and temporal B-splines.[27–29] In many tracer experiments, a compartmental model[7,30] can accurately describe tracer kinetics by use of a system of first-order differential equations. Previously, maximum-likelihood approaches for direct reconstruction of kinetic model parameter images from PET data have been presented.[31,32] Recently Kamasak *et al.*[33] presented a Bayesian approach for dynamic PET that directly reconstructs images of the compartmental model's parameter images by using all the data while imposing spatial regularization. This approach results in substantially improved accuracy compared with previous dynamic imaging methods that do not directly reconstruct the kinetic parameter images.

Here we present a Bayesian, three-dimensional reconstruction approach for time-varying FODT problems with nonlinear parameterizations of some known functional form. We demonstrate the method in a simulation study for the important case of a double exponential model, where the unknown parameters are the two amplitude coefficients and the two rate constants. This case can arise from a compartmental model in some applications, and it is similar to the behavior observed by Gurfinkel *et al.*[11] and Cuccia *et al.*[13] The reconstruction approach is closely related to the methods of Kamasak *et al.*[33] in that it uses a statistical framework to directly reconstruct kinetic model parameters and a similar optimization scheme. We use all of the measured data to reconstruct the model parameter images directly rather than reconstructing and storing a time sequence of fluorescence images. Our approach explicitly accounts for the fact that different sources are illuminated at different times. We also draw upon our recent work, in which we presented a nonlinear Bayesian inversion approach for the ODT and FODT problems and applied it to experimental data.[15,34–36] We use parametric iterative coordinate descent (PICD) optimization,[33,34,37] which is efficient and convenient for enforcing nonnegativity constraints, and we use the generalized Gaussian Markov random field prior model[38] for spatial regularization in the parameter images.

2. FORWARD PROBLEM

A. Diffusion Model

Here we briefly review the forward model for the FODT problem, which we have presented before.[15,34] In applications where scattering dominates over absorption, the transport of light modulated at an RF frequency ω through a scattering medium can be modeled by using a photon diffusion equation.[18,39] For $\exp(j\omega t)$ time variation, it is given by

$$\nabla \cdot [D(r)\,\nabla\,\phi(r,\omega)] - [\mu_a(r) + j\omega/c]\phi(r,\omega) = -\,\delta(r - s_k), \tag{1}$$

where $\phi(r,\omega)$ (W/cm^2) is the complex modulation envelope of the photon flux, s_k is the location of a point source, and $\delta(r)$ is the Dirac function. The diffusion coefficient $D(r)$ (cm) is inversely related to the scattering coefficient, and $\mu_a(r)$ (cm^{-1}) is the absorption coefficient.

For the case where the scattering medium contains a fluorophore, the fluorophore is excited with light at wavelength λ_x and emits light at a longer wavelength λ_m. We use two coupled diffusion equations to describe a fluorescence measurement, with the first to represent λ_x excitation and the second to represent the emitted λ_m photons:[16,17,40]

$$\nabla \cdot [D_x(r)\,\nabla\,\phi_x(r,\omega)] - [\mu_{a_x}(r) + j\omega/c]\phi_x(r,\omega) = -\,\delta(r - s_k), \tag{2}$$

$$\nabla \cdot [D_m(r)\,\nabla\,\phi_m(r,\omega)] - [\mu_{a_m}(r) + j\omega/c]\phi_m(r,\omega) = -\,\phi_x(r,\omega)\,\eta\mu_{a_f}(r)\frac{1 - j\omega\tau(r)}{1 + [\omega\tau(r)]^2}, \tag{3}$$

where the subscripts x and m denote excitation and emission wavelengths λ_x and λ_m, respectively. The fluorescent lifetime $\tau(r)(s)$ is the fluorophore's characteristic exponential decay constant. The fluorescent yield $\eta\mu_{a_f}(r)$ (cm^{-1}) incorporates the fluorophore's quantum efficiency η and its absorption coefficient μ_{a_f}. We will use the notation η, rather than $\eta\mu_{a_f}$, for brevity.

B. Time-Varying Fluorescence

Suppose the fluorescent yield $\eta(r,t)$ varies with time, on a scale comparable to the total acquisition time of the tomography instrument. The time variation might be a result of drug kinetics, which may be of physiological interest. Here we consider the case where $\eta(r,t)$ can be expressed as a (possibly nonlinear) function of U parameters that do not vary in time:

$$\eta(r,t) = \tilde{\eta}(\gamma_1(r),\ldots,\gamma_U(r),t), \tag{4}$$

where $\tilde{\eta}$ is a known function.

One important case that follows this framework is the compartmental model.[30] In a compartmental model, the body consists of a number of compartments, conceptual regions where the drug's concentration is assumed to be uniform. A system of differential equations describes the exchange of the drug among the different compartments. Previously,[11,13] the pharmacokinetics of ICG in animal subjects has been described by use of a three-compartment model, depicted in Fig. 1. The compartments were the plasma, the tissue (the extracellular, extravascular space), and the kidneys and liver, which tend to clear the fluorophore out of the blood pool. Let $c_P(t)$ and $c_T(t)$ be the concentration of fluorophore in the plasma and tissue compartments, respectively. Cuccia *et al.*[13] initially assumed a biexponential decay model for $c_P(t)$ but

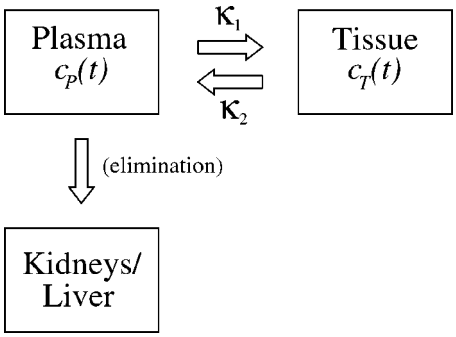

Fig. 1. Compartmental model describing the exchange of contrast agent between the tissue and the plasma.

ultimately observed only single exponential behavior in their experiment owing to the relatively long elimination time of ICG compared with their measurement duration. Hence we will assume single exponential decay for $c_P(t)$,

$$c_P = A\exp(-\kappa_3 t), \tag{5}$$

where A is taken to be the initial fluorophore concentration in the plasma and κ_3 is the rate constant for fluorophore elimination. We assume that the plasma input function does not vary throughout the imaging domain, i.e., that $c_T(t)$ is not large enough to effect the overall rate of elimination significantly. A similar assumption was made by Cuccia *et al.*[13] We also let κ_1 and κ_2 be the rate constants for ICG entering and leaving the tissue. Then the concentrations are obtained by solving a differential equation for $c_T(t)$:

$$\mathrm{d}c_T/\mathrm{d}t = \kappa_1 c_P - \kappa_2 c_T. \tag{6}$$

To obtain a volumetric image, we solve Eq. (6) with initial condition $c_T(0)=0$ to obtain $c_T(t)$ in each voxel:

$$c_T = \left(\frac{\kappa_1 A}{\kappa_2 - \kappa_3}\right)[\exp(-\kappa_3 t) - \exp(-\kappa_2 t)]. \tag{7}$$

The experimentally observed fluorescent yield is proportional to the concentration of fluorophore in the imaging domain. Within each voxel, the fluorophore concentration is some weighted sum of the tissue and blood compartments. Hence we may write $\eta(r,t)$ as

$$\eta(r,t) = w_P(r)c_P(t) + w_T(r)c_T(r,t). \tag{8}$$

Substituting Eqs. (5) and (7) into Eq. (8) yields the biexponential solution,

$$\eta(r,t) = \gamma_1(r)\exp[-\gamma_4(r)t] - \gamma_2(r)\exp[-\gamma_3(r)t], \tag{9}$$

where

$$\gamma_1 = A\left(w_P + \frac{w_T\kappa_1}{\kappa_2 - \kappa_3}\right), \tag{10}$$

$$\gamma_2 = A\left(\frac{w_T\kappa_1}{\kappa_2 - \kappa_3}\right), \tag{11}$$

$$\gamma_3 = \kappa_2, \tag{12}$$

$$\gamma_4 = \kappa_3. \tag{13}$$

From $\gamma_1,\ldots,\gamma_4$, it is possible to obtain the parameters κ_2, κ_3, (Aw_P), and $(Aw_T\kappa_1)$. Hence, we directly reconstruct images of the biexponential model parameters γ_1, γ_2, γ_3, and γ_4. To enforce the spatial independence of $c_P(t)$, one can constrain γ_4 to be the same everywhere. Alternatively, one can reconstruct $\gamma_4(r)$ to check the self-consistency of the model.

Strictly speaking, the time dependence of $\eta(r,t)$ should correspond to a time-dependent perturbation in μ_{a_x}. In previous work, we have observed that perturbational changes in μ_{a_x} do not have a strong effect on reconstructed fluorescence.[15] Hence, for simplicity, we will not consider the reconstruction of time-varying μ_{a_x} here.

C. Tomography Problem

Previously, for the stationary case, we have shown how to reconstruct $\mu_{a_x}(r)$, $\mu_{a_m}(r)$, $D_x(r)$, $D_m(r)$, $\tau(r)$, and $\eta(r)$.[15,34] Here we assume that $\mu_{a_x}(r)$, $\mu_{a_m}(r)$, $D_x(r)$, and $D_m(r)$ are known in advance and do not vary with time, and we consider the problem of reconstructing $\tau(r)$ and $\eta(r,t)$ in the time-varying case.

Suppose that measurements are recorded at C measurement times, which we call $t_1,\ldots,t_C$. At each measurement time, measurements are recorded with one or more sources at wavelength λ_x and detectors are filtered at λ_m. Figure 2 schematically depicts the measurement, with a source and an array of detectors arranged around the domain at each time. Note that the source and detector geometry may be different at different time indices. In particular, practical instruments often illuminate sources sequentially one at a time, whereas all detectors are used simultaneously at all times, and all are fixed in space.

Consider a domain discretized into N volume elements, or voxels. Let r_i denote the position of the ith-voxel centroid. Assuming that $\eta(r,t)$ can be expressed with Eq. (4), we define the image vector x,

$$x = [x_{(0)}^T\ x_{(1)}^T\ \cdots\ x_{(U)}^T]^T, \tag{14}$$

where

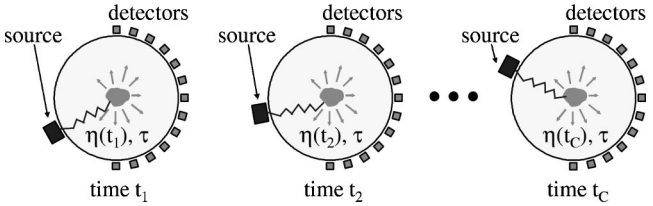

Fig. 2. Measurement approach for reconstructing $\eta(t)$ and τ. Note that the measurement geometry may differ at each time.

$$x_{(u)}^T = [x_{(u),1} \ \cdots \ x_{(u),N}]^T, \tag{15}$$

$$x_{(0)}^T = [\tau(r_1) \ \cdots \ \tau(r_N)]^T, \tag{16}$$

and, for $1 \leqslant u \leqslant U$,

$$x_{(u)}^T = [\gamma_u(r_1) \ \cdots \ \gamma_u(r_N)]^T, \tag{17}$$

with the superscript T denoting the transpose operation. Note that x is of size $(U+1)\times N$, consisting of $U+1$ concatenated parameter vectors of size N. In the parameterization of Eq. (9), $U=4$.

3. INVERSE PROBLEM

A. Bayesian Framework

Let y denote the measurement vector whose ordering will be precisely specified in Subsection 3.B. Similarly, let $f(x)$ denote the forward model. As previously,[15,35,36] we address the ill-posed problem of estimating x from y in a Bayesian framework. The maximum *a posteriori* (MAP) estimate can be computed as

$$\hat{x}_{\mathrm{MAP}} = \underset{x \geqslant 0}{\operatorname{argmax}}\{\log p_{Y|X}(y|x) + \log p_X(x)\}, \tag{18}$$

where $p_{Y|X}(y|x)$ is the data likelihood and $p_X(x)$ is the prior density for the image. We impose positivity constraints for x and also require that $\eta(r_i,t) \geqslant 0$ for all r_i and t. For $p_{Y|X}(y|x)$, we use an independent Gaussian distribution derived from a shot-noise model:[41]

$$p_{Y|X}(y|x) = \frac{1}{(\pi\alpha)^P|\Lambda|^{-1}}\exp\left[-\frac{\|y-f(x)\|_\Lambda^2}{\alpha}\right], \tag{19}$$

where α is a scalar parameter that scales the noise variance, P is the number of measurements, $\|w\|_\Lambda^2 = w^H\Lambda w$ (where H denotes Hermitian transpose), and $\alpha\Lambda^{-1}$ is the covariance matrix given by

$$\alpha\Lambda^{-1} = \alpha\,\mathrm{diag}[|y_1|,|y_2|,\ldots|y_P|]. \tag{20}$$

The prior model $p_X(x)$ is the generalized Gaussian Markov random field model.[38,41] We use upper case to represent the corresponding random variables, and we assume that $X_{(0)},\ldots X_{(U)}$ are independent:

$$p_X(x) = \prod_{u=0}^{U} p_{X_{(u)}}(x_{(u)}) = \prod_{u=0}^{U} \frac{1}{\sigma_{(u)}^N \zeta(\rho_{(u)})} \tag{21}$$

$$\times\exp\left(-\frac{1}{\rho_{(u)}\sigma_{(u)}^{\rho_{(u)}}}\sum_{\{i,j\}\in\mathcal{N}} b_{i-j}|x_{(u),i}-x_{(u),j}|^{\rho_{(u)}}\right), \tag{22}$$

where the u subscripts correspond to Eq. (15), $\mathcal{N}$ consists of all pairs of neighboring (adjacent) nodes in a 26-neighbor system, and b_{i-j} is the weighting coefficient corresponding to the ith and jth nodes. The coefficients b_{i-j} are assigned to be inversely proportional to the node separation in a cube-shaped node layout, where $\Sigma_j b_{i-j}=1$. The parameters ρ and σ control the shape and scale of the distribution, and $\zeta(\rho)$ is a normalization term.

We incorporate α into the inverse problem as an unknown instrument parameter, as we have found that this tends to improve the robustness and speed of convergence:[42]

$$\hat{x} = \arg\max_{x\geqslant 0,\alpha\geqslant 0}\{p_{X|Y}(x|y,\alpha)\}. \tag{23}$$

We form the log posterior probability $l(x)$,[42]

$$l(x) = -P\log\|y-f(x)\|_\Lambda^2 - \sum_{u=0}^{U}\left(\frac{1}{\rho_{(u)}\sigma_{(u)}^{\rho_{(u)}}}\sum_{\{i,j\}\in\mathcal{N}} b_{i-j}|x_{(u),i}-x_{(u),j}|^{\rho_{(u)}}\right), \tag{24}$$

and implement its maximization by alternating closed-form updates of $\hat{\alpha}$ with updates of $\hat{x}$:

$$\hat{\alpha} \leftarrow \frac{1}{P}\|y-f(\hat{x})\|_\Lambda^2 \tag{25}$$

$$\hat{x} \leftarrow \arg\ \underset{x\geqslant 0}{\mathrm{update}}\{\log p_{Y|X}(y|x,\hat{\alpha}) + \log p_X(x)\}, \tag{26}$$

where $\leftarrow$ denotes assignment and arg update denotes an iteration of some optimizer.

The update in relation (26) is equivalent to reducing a cost function

$$c(x,\hat{\alpha}) = \frac{1}{\hat{\alpha}}\|y-f(x)\|_\Lambda^2 + \sum_{u=0}^{U}\left(\frac{1}{\rho_{(u)}\sigma_{(u)}^{\rho_{(u)}}}\sum_{\{i,j\}\in\mathcal{N}} b_{i-j}|x_{(u),i}-x_{(u),j}|^{\rho_{(u)}}\right). \tag{27}$$

B. Definitions

Define $s_{t_c,k}$ as the location of the kth source at time t_c, and $d_{t_c,m'}$ as the location of the m'th detector at time t_c, and let $g_x(s_{t_c,k},d_{t_c,m'};\omega)$ and $g_m(s_{t_c,k},d_{t_c,m'};\omega)$ be the diffusion equation Green's functions for wavelength λ_x and λ_m, respectively. Also, let $\phi_f(s_{t_c,k},d_{t_c,m'};\omega,t_c,x)$ be the fluorescence observed at observation position $d_{t_c,m'}$ for an excitation source at $s_{t_c,k}$, where

$$\phi_f(s_{t_c,k},d_{t_c,m'};\omega,t_c,x) = \int \eta(r,t_c)\frac{1-j\omega\tau(r)}{1+[\omega\tau(r)]^2} \times g_x(s_{t_c,k},r;\omega)g_m(r,d_{t_c,m'};\omega)\mathrm{d}^3r. \tag{28}$$

Suppose that at time t_c we have K_c sources and M_c detectors at a modulation frequency of ω. (Typically, $K_c=1$ for most systems that illuminate sources sequentially.) Let $f_{\omega,t_c}(x)$ be the forward model for the data taken at t_c with $\exp(j\omega t)$-modulated light. Then

$$f_{\omega,t_c}(x_f)=\begin{bmatrix}\phi_f\left(s_{t_c,1},d_{t_c,1};\omega,t_c,x\right)\\ \phi_f\left(s_{t_c,1},d_{t_c,2};\omega,t_c,x\right)\\ \vdots\\ \phi_f\left(s_{t_c,1},d_{t_c,M_c};\omega,t_c,x\right)\\ \phi_f\left(s_{t_c,2},d_{t_c,1};\omega,t_c,x\right)\\ \vdots\\ \phi_f\left(s_{t_cK_c},d_{t_c,M_c};\omega,t_c,x\right)\end{bmatrix}. \tag{29}$$

Let Q be the number of modulation frequencies used and C be the number of measurement times. Then

$$f_{t_c}(x)=\left[f_{\omega_1,t_c}(x)^T,f_{\omega_2,t_c}(x)^T\ldots f_{\omega_Q,t_c}(x)^T\right]^T, \tag{30}$$

$$f(x)=\left[f_{t_1}(x)^T,f_{t_2}(x)^T\ldots f_{t_C}(x)^T\right]^T. \tag{31}$$

Similarly, we define the measurement vector y as

$$y_{t_c}=\left[y_{\omega_1,t_c}^T,y_{\omega_2,t_c}^T\cdots y_{\omega_Q,t_c}^T\right]^T, \tag{32}$$

$$y=\left[y_{t_1}^T,y_{t_2}^T\ldots y_{t_C}^T\right]^T, \tag{33}$$

corresponding to the same order used in Eq. (31). Note that $g(s_k,d_{m'},\omega)=g(d_{m'},s_k,\omega)$ at λ_x and at λ_m, owing to reciprocity.[43]

We may use matrices to approximate the integration of Eq. (28). For consistency, we assume a regular rectangular mesh in the following formulation, although we note that more generic finite-element formulations of similar problems have been presented previously.[44] We define

$$G^x(\omega,t_c)=\begin{bmatrix}g_x\left(s_{t_c,1},r_1;\omega\right) & \cdots & g_x\left(s_{t_c,1},r_N;\omega\right)\\ \vdots & \ddots & \vdots\\ g_x\left(s_{t_c,K},r_1;\omega\right) & \cdots & g_x\left(s_{t_c,K},r_N;\omega\right)\end{bmatrix}, \tag{34}$$

$$G^m(\omega,t_c)=\begin{bmatrix}g_m\left(d_{t_c,1},r_1;\omega\right) & \cdots & g_m\left(d_{t_c,1},r_N;\omega\right)\\ \vdots & \ddots & \vdots\\ g_m\left(d_{t_c,M},r_1;\omega\right) & \cdots & g_m\left(d_{t_c,M},r_N;\omega\right)\end{bmatrix}. \tag{35}$$

We also define J_{ω,t_c} as

$$J_{\omega,t_c}=V\begin{bmatrix}G^x_{1,1}(\omega,t_c)G^m_{1,1}(\omega,t_c) & \cdots & G^x_{1,N}(\omega,t_c)G^m_{1,N}(\omega,t_c)\\ \vdots & \ddots & \vdots\\ G^x_{1,1}(\omega,t_c)G^m_{M,1}(\omega,t_c) & \cdots & G^x_{1,N}(\omega,t_c)G^m_{M,N}(\omega,t_c)\\ G^x_{2,1}(\omega,t_c)G^m_{1,1}(\omega,t_c) & \cdots & G^x_{2,N}(\omega,t_c)G^m_{1,N}(\omega,t_c)\\ \vdots & \ddots & \vdots\\ G^x_{K,1}(\omega,t_c)G^m_{M,1}(\omega,t_c) & \cdots & G^x_{K,N}(\omega,t_c)G^m_{M,N}(\omega,t_c)\end{bmatrix}, \tag{36}$$

where V is the volume of a voxel. Let

$$h(x_{(*),i},\omega,t)=\eta(r_i,t)\frac{1-j\omega\tau(r_i)}{1+[\omega\tau(r_i)]^2}, \tag{37}$$

$$h_{\omega,t_c}(x)=\left[h(x_{(*),1},\omega,t_c)\ \cdots\ h(x_{(*),N},\omega,t_c)\right]^T, \tag{38}$$

where $x_{(*),n}=[\tau(r_n)\ \gamma_1(r_n)\ \cdots\ \gamma_U(r_n)]^{\mathrm{T}}$. Then

$$f_{\omega,t_c}(x)=J_{\omega,t_c}h_{\omega,t_c}(x) \tag{39}$$

if we ignore discretization error. Therefore Eq. (27) is equivalent to

$$c(x,\hat{\alpha})=\frac{1}{\hat{\alpha}}\sum_{c=1}^{C}\sum_{q=1}^{Q}\left\|y_{\omega_q,t_c}-J_{\omega_q,t_c}h_{\omega_q,t_c}(x)\right\|^2_{\Lambda_{\omega_q,t_c}}+\sum_{u=0}^{U}\frac{1}{\rho_{(u)}\sigma_{(u)}^{\rho_{(u)}}}\sum_{\{i,j\}\in\mathcal{N}}b_{i-j}|x_{(u),i}-x_{(u),j}|^{\rho_{(u)}}. \tag{40}$$

The cost function in Eq. (40) is used in our image reconstruction.

C. Parametric Iterative Coordinate Descent

To optimize Eq. (40), we use an algorithm that we call parametric iterative coordinate descent (PICD). It is based on earlier work,[41] and it is modified to allow for computationally efficient updates of the kinetic model parameters. The voxels are individually updated in random order by optimizing the cost function with respect to the parameters at each voxel position. The updates enforce the constraints $x\geq 0$, and also $\gamma_1\geq\gamma_2$ and $\gamma_3\geq\gamma_4$, which are necessary and sufficient to ensure that each parameter is nonnegative and that $\eta(t)\geq 0$ for all time.

In one update scan for $\hat{x}$, all of the unknowns $x_{(u)}$, $u=0,\ldots 4$ are updated at all N voxel positions. Let the scalar $x_{(u),i}$ denote the ith element of $x_{(u)}$. With all other image elements fixed, the PICD update for the estimate $\hat{x}_{(u),i}$ is given by

$$\hat{x}_{(u),i}\leftarrow\arg\min_{x_{(u),i}\geq 0}\left\{\frac{1}{\hat{\alpha}}\sum_{c=1}^{C}\sum_{q=1}^{Q}\left\|y_{\omega_q,t_c}-\left[J_{\omega_q,t_c}\right]_{*(i)}h(x_{(*),i},\omega_q,t_c)\right\|^2_{\Lambda_{\omega_q,t_c}}+\frac{1}{\rho_{(u)}\sigma_{(u)}^{\rho_{(u)}}}\sum_{j\in\mathcal{N}_i}b_{i-j}|x_{(u),i}-\hat{x}_{(u),j}|^{\rho_{(u)}}\right\}, \tag{41}$$

where $\mathcal{N}_i$ is the set of nodes neighboring node i and $\rho_{(u)}$ and $\sigma_{(u)}$ are the prior model parameters for $X_{(u)}$. In relation (41), $[J_{\omega_q,t_c}]_{*(i)}$ denotes the ith column of J_{ω_q,t_c}. Suppose we have an initial guess $\tilde{x}$, and let $z_{\omega_q,t_c}=y_{\omega_q,t_c}-f_{\omega_q,t_c}(\tilde{x})$. Then Eq. (41) is equivalent to

$$\hat{x}_{(u),i} \leftarrow \arg\min_{x_{(u),i}\geq 0} \left\{ \frac{1}{\hat{\alpha}} \sum_{c=1}^{C} \sum_{q=1}^{Q} \| z_{\omega_q,t_c} - [J_{\omega_q,t_c}]_{*(i)} [h(x_{(*),i},\omega_q,t_c) - h(\tilde{x}_{(*),i},\omega_q,t_c)] \|^2_{\Lambda_{\omega_q,t_c}} + \frac{1}{\rho_{(u)}\sigma_{(u)}{}^{\rho_{(u)}}} \sum_{j\in\mathcal{N}_i} b_{i-j} |x_{(u),i} - \hat{x}_{(u),j}|^{\rho_{(u)}} \right\},$$

$$= \arg\min_{x_{(u),i}\geq 0} \left\{ \frac{1}{\hat{\alpha}} \sum_{c=1}^{C} \sum_{q=1}^{Q} \left(\theta_{1,\omega_q,t_c} [h(x_{(*),i},\omega_q,t_c) - h(\tilde{x}_{(*),i},\omega_q,t_c)] + \frac{\theta_{2,\omega_q,t_c}}{2} [h(x_{(*),i},\omega_q,t_c) - h(\tilde{x}_{(*),i},\omega_q,t_c)]^2 \right) + \frac{1}{\rho_{(u)}\sigma_{(u)}{}^{\rho_{(u)}}} \sum_{j\in\mathcal{N}_i} b_{i-j} |x_{(u),i} - \tilde{x}_{(u),j}|^{\rho_{(u)}} \right\}, \quad (42)$$

where

$$\theta_{1,\omega_q,t_c} = -2\,\mathrm{Re}\{[J_{\omega_q,t_c}]^H_{*i} \Lambda_{\omega_q,t_c} z_{\omega_q,t_c}\}, \quad (43)$$

$$\theta_{2,\omega_r,t_c} = 2[J_{\omega_q,t_c}]^H_{*i} \Lambda_{\omega_q,t_c} [J_{\omega_q,t_c}]_{*i}. \quad (44)$$

In relation (42), θ_{1,ω_q,t_c} and θ_{2,ω_q,t_c} are not functions of $x_{(u),i}$ and thus do not need to be recomputed during the nonlinear, one-dimensional line search over $x_{(u),i}$. This property enables significant computational savings, as repeated computations of θ_{1,ω_q,t_c} and θ_{2,ω_q,t_c} would require numerous complex multiplications. We perform the minimization over $x_{(u),i}$ by use of a Golden Section search.[45]

To enforce the constraints $\gamma_1 \geq \gamma_2$, we initially perform minimizations over $x_{(1),i}$ and over $x_{(2),i}$ and observe whether the inequality constraint is satisfied. If $\hat{x}_{(2),i} > \hat{x}_{(1),i}$, we perform a new line search enforcing $x_{(1),i} = x_{(2),i}$:

$$\hat{x}_{(1),i}, \hat{x}_{(2),i} \leftarrow \arg\min_{x_{(1),i}=x_{(2),i}\geq 0} \left\{ \frac{1}{\hat{\alpha}} \sum_{c=1}^{C} \sum_{q=1}^{Q} \left(\theta_{1,\omega_q,t_c} [h(x_{(*),i},\omega_q,t_c) - h(\tilde{x}_{(*),i},\omega_q,t_c)] + \frac{\theta_{2,\omega_q,t_c}}{2} [h(x_{(*),i},\omega_q,t_c) - h(\tilde{x}_{(*),i},\omega_q,t_c)]^2 \right) + \frac{1}{\rho_{(1)}\sigma_{(1)}{}^{\rho_{(1)}}} \sum_{j\in\mathcal{N}_i} b_{i-j} |x_{(1),i} - \tilde{x}_{(1),j}|^{\rho_{(1)}} + \frac{1}{\rho_{(2)}\sigma_{(2)}{}^{\rho_{(2)}}} \sum_{j\in\mathcal{N}_i} b_{i-j} |x_{(2),i} - \tilde{x}_{(2),j}|^{\rho_{(2)}} \right\}. \quad (45)$$

A similar procedure is used to enforce the $\gamma_3 \geq \gamma_4$ condition.

We implement the joint estimation of α and x iteratively. One iteration consists of a closed-form update of $\hat{\alpha}$ by use of Eq. (25), followed by a PICD scan to update $\hat{x}$.

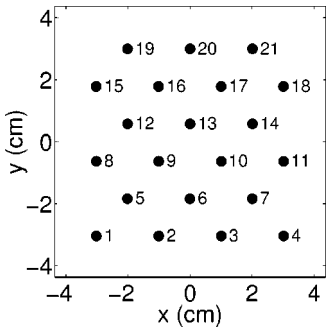

Fig. 3. Source and detector locations used in the simulations. The sources were on the bottom face of the phantom, and the detectors were on the top. The sources were illuminated in the order shown, with one source used for each measurement time.

Appendix A provides pseudocode for a more detailed specification of the PICD algorithm.

4. SIMULATION

To validate the method, we performed a simulation study. A synthetic time series of data was generated from a cube-shaped phantom containing two heterogeneities. The background properties were $\mu_{a_x} = \mu_{a_m} = 0.047\ \mathrm{cm}^{-1}$ and $D_x = D_m = 0.027$ cm. The heterogeneities had the same τ but different γ_1, γ_2, and γ_3. The parameter γ_4 was 0 and was not reconstructed. This corresponds to an assumption that the elimination time of fluorophore from the plasma is long compared with the measurement time, which is reasonable in cases where we are most interested in the initial drug uptake behavior. The parameter values were selected to result in uptake behavior on the order of seconds, which may be reasonable for a small-animal imaging experiment.[13]

The phantom was 8 cm × 8 cm × 5.7 cm in size, and it was discretized into 33 × 33 × 17 voxels of size 0.26 cm × 0.26 cm × 0.38 cm. To generate the synthetic measurements, we solved the diffusion equation numerically by using multigrid finite differences[46] and extrapolated zero-flux boundary conditions with interpolated source positions, as we have described previously.[36] The simulation used a modulation frequency of 78.4 MHz. Figure 3 shows the locations of the sources that were placed on the bottom face of the domain. The same positions were used as detector positions on the top face of the domain, simulating a parallel-plate transmission geometry similar to that which has been used for optical mammography previously. The sources were illuminated one at a time at different times, in the order shown in Fig. 3, and the data consisted of one complete pass through all of the sources, with 441 measurements in all. Simulated shot noise was added, giving an average signal to-noise ratio of 28 dB for all the data. The true phantom is shown in Fig. 4, with cross-section images through each of the heterogeneities.

For the reconstructions, the hyperparameter ρ was set to 2, corresponding to the Gaussian Markov random field model. Although automatic estimation of the hyperparameters is possible in principle,[47] we chose σ to give the best empirical results, as we have done previously.[34] For this problem the best results were given by $\sigma_{(0)} = 2.75 \times 10^{-10}$, $\sigma_{(1)} = 0.5$, $\sigma_{(2)} = 0.5$, and $\sigma_{(3)} = 0.0125$ (where the

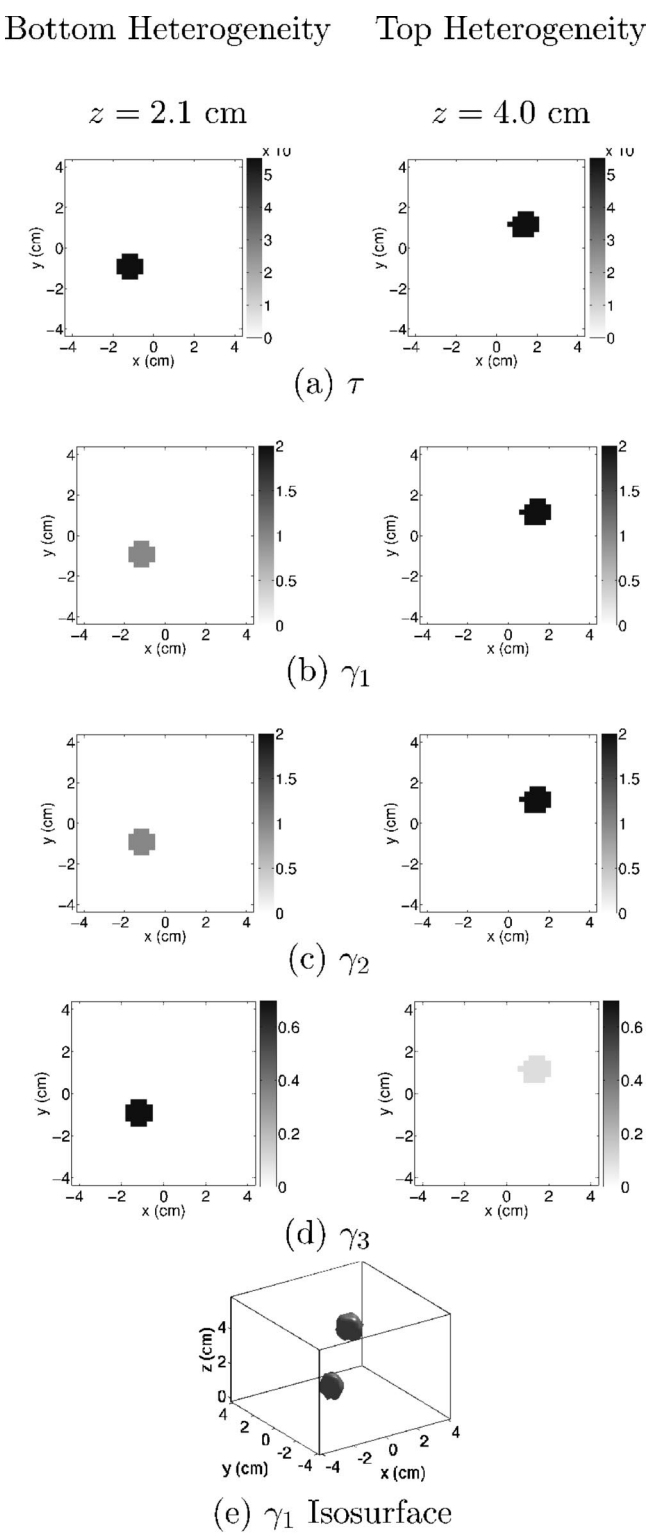

Fig. 4. True parameter images describing the time-varying fluorescence in the simulation study. Cross sections are shown through the top heterogeneity and the bottom heterogeneity. Note that the parameter γ_3 indicates different uptake rates in the two heterogeneities. In (e), an isosurface of the γ_1 reconstruction is shown, contoured at 1/3 of the maximum value.

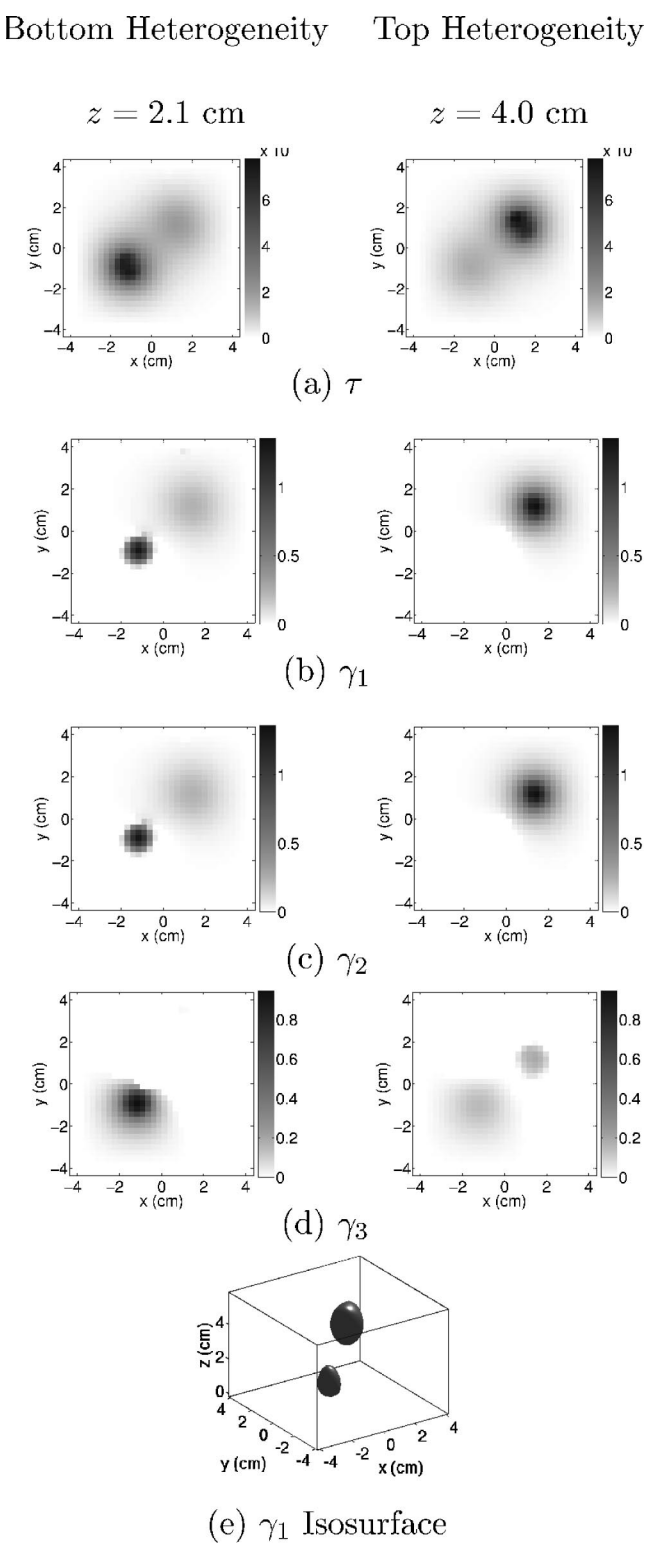

Fig. 5. Reconstructed parameter images describing the time-varying fluorescence in the simulation study. In (e), an isosurface of the γ_1 reconstruction is shown, contoured at 1/3 of the maximum value.

units of lifetime are seconds and the units of fluorescence are cm^{-1}). The PICD algorithm was run to 50 iterations, which required approximately 2 hours on a 2 GHz American Micro Devices Athlon workstation.

The reconstructed parametric images are shown in Fig. 5. The results are accurate, although shadowing effects are apparent in the images. In particular, γ_3, which is related to a dye's uptake rate, was reconstructed accurately, enabling a clear distinction between the two objects. Fig-

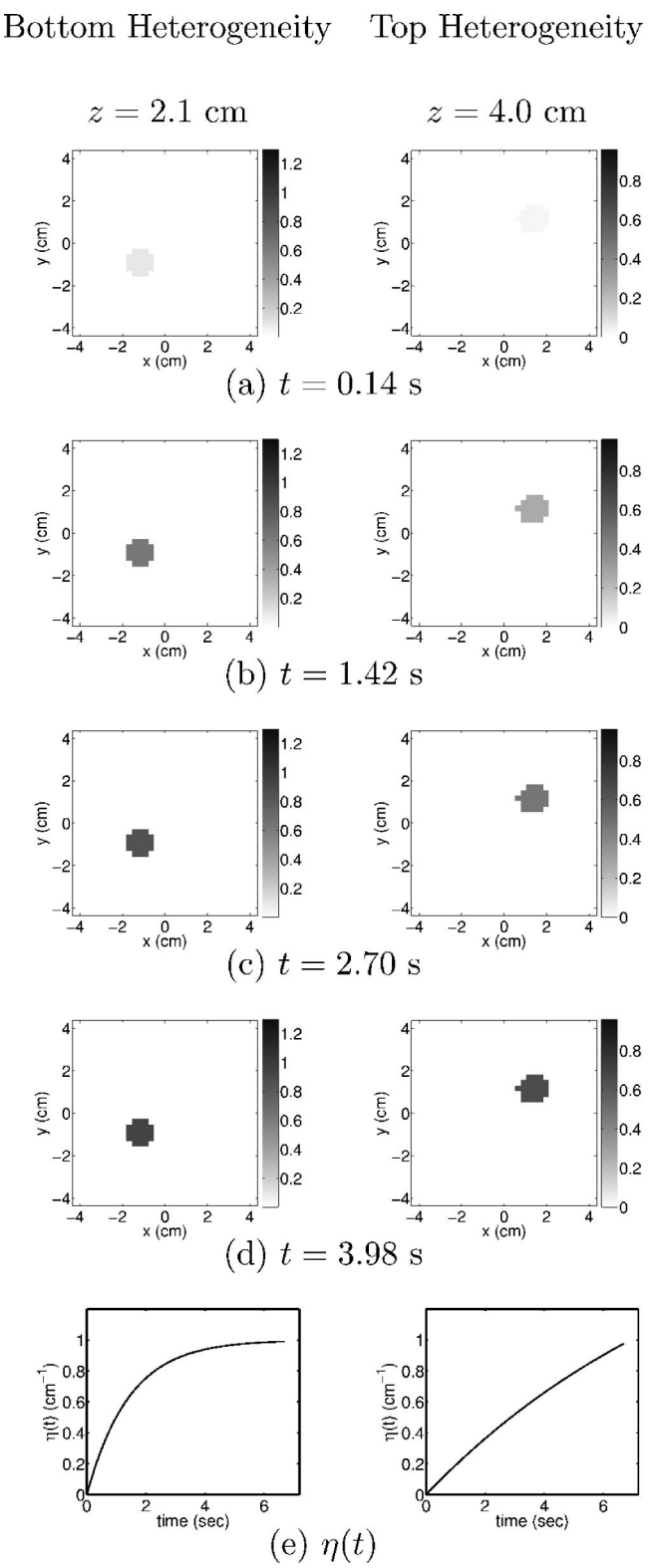

Fig. 6. (a)–(d) True fluorescence versus time $\eta(t)$. (e) $\eta(t)$ for a sample point within each heterogeneity.

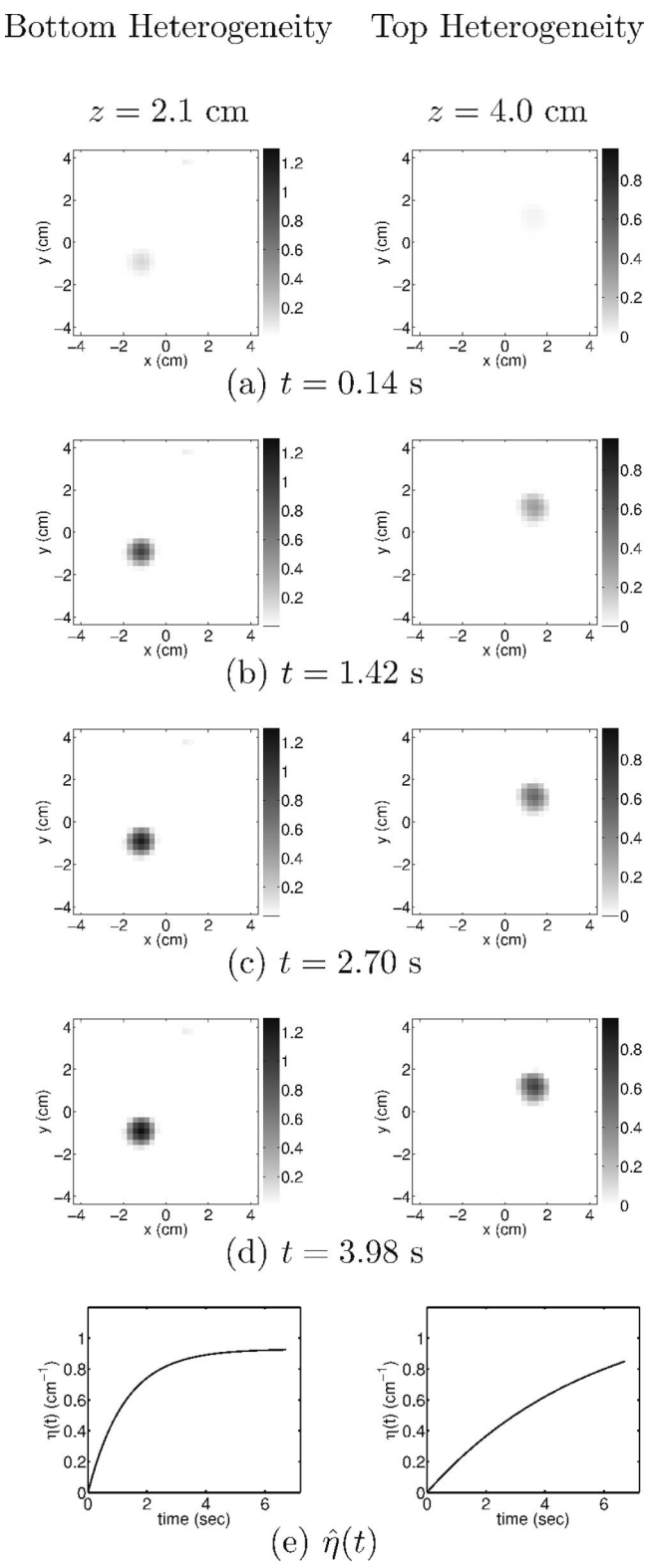

Fig. 7. (a)–(d) Fluorescence versus time, reconstructed by parametric ICD method. (e) $\hat{\eta}(t)$ for a sample point within each heterogeneity.

ures 6(a)–6(d) show the true images of $\eta(r,t)$ for the two objects, at four different times, and Fig. 6(e) shows plots of $\eta(t)$ for a single point near the center of each object. The reconstructed time variation is also accurate, without shadowing artifacts.

The reconstruction $\hat{\eta}(r,t)$ was obtained by substituting $\hat{\gamma}_1(r)$, $\hat{\gamma}_2(r)$, and $\hat{\gamma}_3(r)$ into Eq. (9). The results shown in Fig. 7 indicate that all features are nicely captured. Figure 8 is a convergence plot showing monotonic decrease of the cost function versus iteration number. For compari-

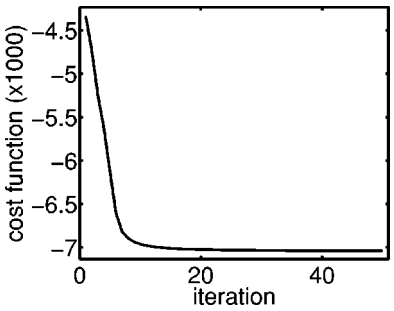

Fig. 8. Convergence for the PICD algorithm in the simulation study.

son, we also reconstructed $\eta(r,t)$ by independently reconstructing $\eta(r,t_i)$ at each measurement time t_i, using our previous FODT reconstruction algorithm.[34] For the first simulation, we used the same 441 measurements that were used for the results in Fig. 9. The reconstructions all used $\rho=2$, with $\sigma=0.5$ for η and $\sigma=2.75\times10^{-10}$ for τ (which gave the best empirical results). We performed 21 reconstructions of $\eta(r,t_i)$, using a single source and 21 detectors for each. The results, shown in Fig. 9, have poor accuracy. For the second simulation, we greatly increased the number of data, using all 21 sources and 21 detectors for each of the reconstructions of $\eta(r,t_i)$ (i.e., 9261 measurements, with 441 measurements used at each time index). The reconstructions in this simulation used $\rho=2$, with $\sigma=0.375$ for η and $\sigma=2.75\times10^{-10}$ for τ. The results are shown in Fig. 10. With this 21-fold increase in data, the reconstructions accuracy approaches that of the parametric imaging method.

5. CONCLUSIONS

We have presented a method for parametric reconstruction of fluorescent drug kinetics by use of fluorescence optical diffusion tomography. The simulation showed that two heterogeneities with different time-dependent behavior could be reconstructed simultaneously and could be clearly distinguished on the basis of uptake-related parameters. In principle, receptor-targeted fluorescent probes may have a significantly faster uptake rate in tumors than in the surrounding tissue. Hence the ability to reconstruct the drug uptake kinetics could facilitate tumor imaging with high contrast in comparison with methods that do not make full use of the drug dynamics.

The presented approach is flexible and may be applied to more sophisticated compartmental models. In principle, more complicated kinetic models that incorporate additional compartments or nonlinear saturation effects may be used in the same framework, as they simply increase the complexity of the single-site updates. In addition, the PICD algorithm may be incorporated into a multigrid framework[48] to improve convergence properties for a wide variety of images.

Experimental demonstration of the approach should be developed in future work. One possibility is that controlled FODT Intralipid phantom experiments using fluorescent contrast agents[34] could be modified for kinetic imaging work. For example, fluorescent dye could be introduced into the phantom over time while the FODT instrument's sources and detectors record measurements. Ultimately, validation on living animal subjects would be required, extending previous kinetic modeling work to full three-dimensional imaging geometries. Recent work with

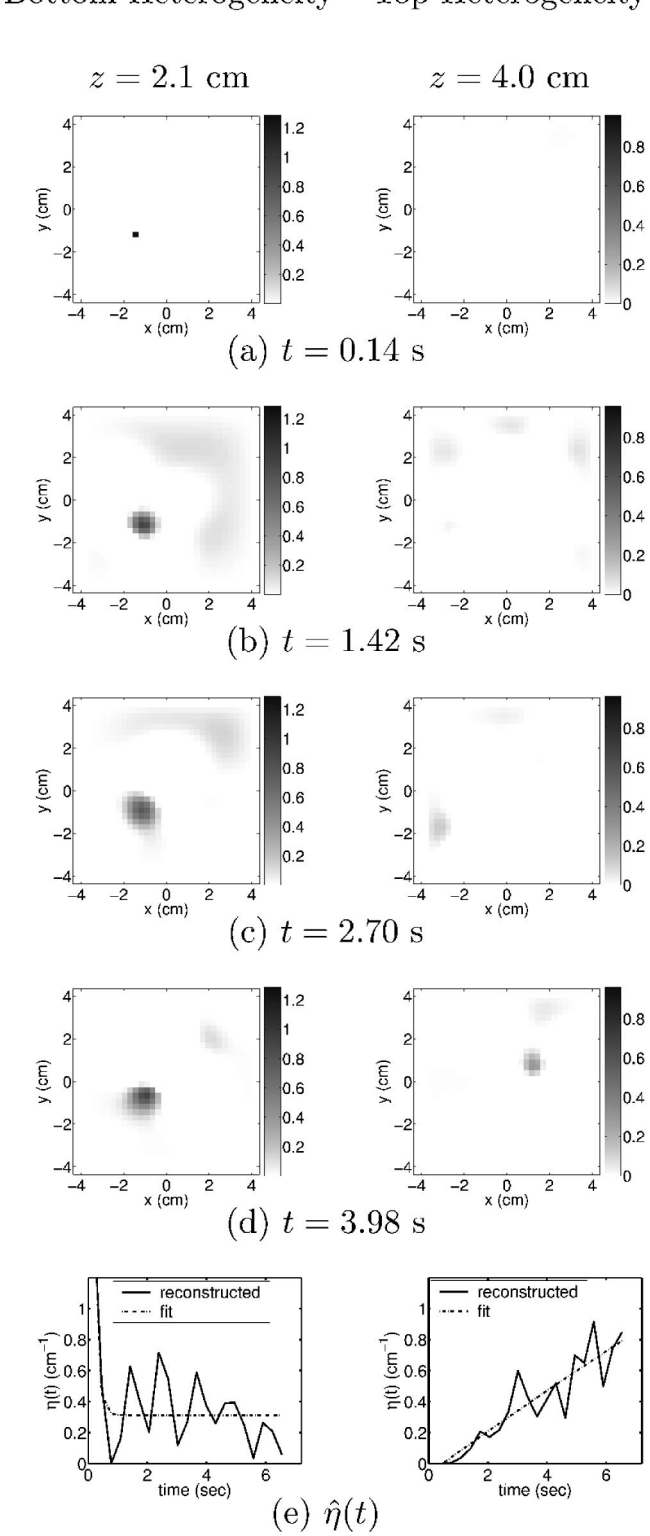

Fig. 9. (a)–(d) Fluorescence versus time, reconstructed independently at each measurement time, with the same data as in the parametric reconstructions. (e) $\hat{\eta}(t)$ for a sample point within each heterogeneity.

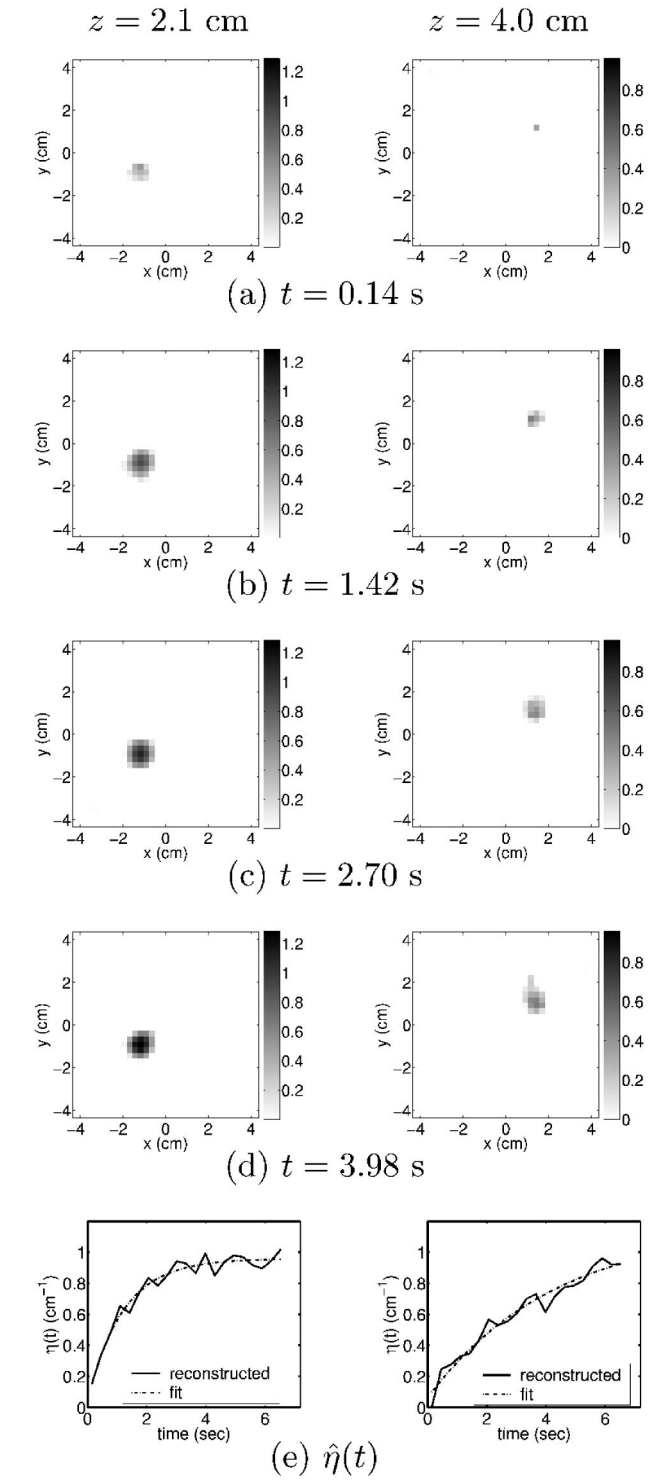

Fig. 10. (a)–(d) Fluorescence versus time, reconstructed independently at each measurement time, with a 21-fold increase in data over those used in the parametric reconstructions. (e) $\hat{\eta}(t)$ for a sample point within each heterogeneity.

three-dimensional fluorophore localization and molecular imaging with animal tissues[49,50] could be applied to the kinetic imaging problem.

APPENDIX A: PSEUDOCODE FOR THE INVERSION ALGORITHM

main {

1. Form $G_x^{(s)}$ and $G_m^{(d)}$
2. Repeat until converged: {
   (a) $\hat{\alpha}_f \leftarrow 1/P_f \|y_f - f_f(\hat{x}_f, \hat{x}_x, \hat{x}_m)\|^2_{\Lambda_f}$
   (b) $\hat{x}_f \leftarrow$ ICD_update$(\hat{x}_f, \hat{\alpha}_f, G_x^{(s)}, G_m^{(d)})$
   }

}

$\hat{x} \leftarrow$ ICD_update$(\hat{x}, \hat{\alpha}, G^{(s)}, G^{(d)}; x)$ {

1. For $c = 1,\ldots,C$ {
   (a) For $q = 1,\ldots,Q$ {
      i. $z_{\omega_q,t_c} \leftarrow y_{\omega_q,t_c} - f_{\omega_q,t_c}(\hat{x})$
   }
   }
2. For $i = 1,\ldots,N$ (in random order), {
   (a) $\tilde{x}_i \leftarrow \hat{x}_i$
   (b) For $c = 1,\ldots,C$ {
      i. For $q = 1,\ldots,Q$ {
         A. Compute $[J_{\omega_q,t_c}]_{*(i)}$, by taking the ith column in Eq. (36)
         B. $\theta_{1,\omega_q,t_c} \leftarrow -2\mathrm{Re}\{[J_{\omega_q,t_c}]^H_{*i} \Lambda_{\omega_q,t_c} z_{\omega_q,t_c}\}$
         C. $\theta_{2,\omega_q,t_c} \leftarrow 2[J_{\omega_q,t_c}]^H_{*i} \Lambda_{\omega_q,t_c} [J_{\omega_q,t_c}]_{*i}$
         }
   }
   (c) $\hat{\tau} \leftarrow \arg\min_{x_{(0),i} \geq 0}$ {

$$\frac{1}{\hat{\alpha}} \sum_{c=1}^{C} \sum_{q=1}^{Q} \Big(\theta_{1,\omega_q,t_c} [h(x_{(*),i}, \omega_q, t_c) - h(\tilde{x}_{(*),i}, \omega_q, t_c)] + \frac{\theta_{2,\omega_q,t_c}}{2} [h(x_{(*),i}, \omega_q, t_c) - h(\tilde{x}_{(*),i}, \omega_q, t_c)]^2 \Big) + \frac{1}{\rho_{(0)} \sigma_{(0)}^{\rho(0)}} \sum_{j \in \mathcal{N}_i} b_{i-j} |x_{(0),i} - \tilde{x}_{(0),j}|^{\rho(0)} \}$$

   (d) $\hat{\gamma}_1 \leftarrow \arg\min_{x_{(1),i} \geq 0}$ {

$$\frac{1}{\hat{\alpha}} \sum_{c=1}^{C} \sum_{q=1}^{Q} \Big(\theta_{1,\omega_q,t_c} [h(x_{(*),i}, \omega_q, t_c) - h(\tilde{x}_{(*),i}, \omega_q, t_c)] + \frac{\theta_{2,\omega_q,t_c}}{2} [h(x_{(*),i}, \omega_q, t_c) - h(\tilde{x}_{(*),i}, \omega_q, t_c)]^2 \Big) + \frac{1}{\rho_{(1)} \sigma_{(1)}^{\rho(1)}} \sum_{j \in \mathcal{N}_i} b_{i-j} |x_{(1),i} - \tilde{x}_{(1),j}|^{\rho(1)} \}$$

   (e) $\hat{\gamma}_2 \leftarrow \arg\min_{x_{(2),i} \geq 0}$ {

$$\frac{1}{\hat{\alpha}} \sum_{c=1}^{C} \sum_{q=1}^{Q} \Big(\theta_{1,\omega_q,t_c} [h(x_{(*),i}, \omega_q, t_c) - h(\tilde{x}_{(*),i}, \omega_q, t_c)] + \frac{\theta_{2,\omega_q,t_c}}{2} [h(x_{(*),i}, \omega_q, t_c) - h(\tilde{x}_{(*),i}, \omega_q, t_c)]^2 \Big) + \frac{1}{\rho_{(2)} \sigma_{(2)}^{\rho(2)}} \sum_{j \in \mathcal{N}_i} b_{i-j} |x_{(2),i} - \tilde{x}_{(2),j}|^{\rho(2)} \}$$

   (f) if $(\hat{\gamma}_2 > \hat{\gamma}_1)$ {

$$\hat{\gamma}_1, \hat{\gamma}_2 \leftarrow \arg\min_{x_{(1),i} = x_{(2),i} \geq 0} \Big\{ \frac{1}{\hat{\alpha}} \sum_{c=1}^{C} \sum_{q=1}^{Q} \Big(\theta_{1,\omega_q,t_c} [h(x_{(*),i}, \omega_q, t_c) - h(\tilde{x}_{(*),i}, \omega_q, t_c)] + \frac{\theta_{2,\omega_q,t_c}}{2} [h(x_{(*),i}, \omega_q, t_c) - h(\tilde{x}_{(*),i}, \omega_q, t_c)]^2 \Big) + \frac{1}{\rho_{(1)} \sigma_{(1)}^{\rho(1)}} \sum_{j \in \mathcal{N}_i} b_{i-j} |x_{(1),i} - \tilde{x}_{(1),j}|^{\rho(1)} + \frac{1}{\rho_{(2)} \sigma_{(2)}^{\rho(2)}} \sum_{j \in \mathcal{N}_i} b_{i-j} |x_{(2),i} - \tilde{x}_{(2),j}|^{\rho(2)} \}$$

}

(g) $\hat{\gamma}_3 \leftarrow \arg\min_{x_{(3),i} \geq 0}$ {

$\frac{1}{\hat{\alpha}} \sum_{c=1}^{C} \sum_{q=1}^{Q} (\theta_{1,\omega_q,t_c}[h(x_{(*),i},\omega_q,t_c) - h(\tilde{x}_{(*),i},\omega_q,t_c)]$

$+ \frac{\theta_{2,\omega_q,t_c}}{2}[h(x_{(*),i},\omega_q,t_c) - h(\tilde{x}_{(*),i},\omega_q,t_c)]^2)$

$+ \frac{1}{\rho_{(3)}\sigma_{(3)}^{\rho(3)}} \sum_{j \in \mathcal{N}_i} b_{i-j} |x_{(3),i} - \tilde{x}_{(3),j}|^{\rho(3)}$ }

(h) $\hat{\gamma}_4 \leftarrow \arg\min_{x_{(4),i} \geq 0}$ {

$\frac{1}{\hat{\alpha}} \sum_{c=1}^{C} \sum_{q=1}^{Q} (\theta_{1,\omega_q,t_c}[h(x_{(*),i},\omega_q,t_c) - h(\tilde{x}_{(*),i},\omega_q,t_c)]$

$+ \frac{\theta_{2,\omega_q,t_c}}{2}[h(x_{(*),i},\omega_q,t_c) - h(\tilde{x}_{(*),i},\omega_q,t_c)]^2)$

$+ \frac{1}{\rho_{(4)}\sigma_{(4)}^{\rho(4)}} \sum_{j \in \mathcal{N}_i} b_{i-j} |x_{(4),i} - \tilde{x}_{(4),j}|^{\rho(4)}$ }

(i) if ($\hat{\gamma}_4 > \hat{\gamma}_3$) {

$\hat{\gamma}_3, \hat{\gamma}_4 \leftarrow \arg\min_{x_{(3),i} = x_{(4),i} \geq 0}$ {

$\frac{1}{\hat{\alpha}} \sum_{c=1}^{C} \sum_{q=1}^{Q} (\theta_{1,\omega_q,t_c}[h(x_{(*),i},\omega_q,t_c) - h(\tilde{x}_{(*),i},\omega_q,t_c)]$

$+ \frac{\theta_{2,\omega_q,t_c}}{2}[h(x_{(*),i},\omega_q,t_c) - h(\tilde{x}_{(*),i},\omega_q,t_c)]^2)$

$+ \frac{1}{\rho_{(3)}\sigma_{(3)}^{\rho(3)}} \sum_{j \in \mathcal{N}_i} b_{i-j} |x_{(3),i} - \tilde{x}_{(3),j}|^{\rho(3)}$

$+ \frac{1}{\rho_{(4)}\sigma_{(4)}^{\rho(4)}} \sum_{j \in \mathcal{N}_i} b_{i-j} |x_{(4),i} - \tilde{x}_{(4),j}|^{\rho(4)}$ }

}

(j) $[\hat{x}_{(0),i}, \hat{x}_{(2),i}, \hat{x}_{(3),i}, \hat{x}_{(4),i}] \leftarrow [\hat{\tau}, \hat{\gamma}_1, \hat{\gamma}_2, \hat{\gamma}_3]$

(k) For $c = 1, \ldots, C$ {

i. For $q = 1, \ldots, Q$ {

A. $z_{\omega_q,t_c} \leftarrow z_{\omega_q,t_c} + [J_{\omega_q,t_c}]_{*i}[h(\hat{x}_{(*),i},\omega_q,t_c) - h(\tilde{x}_{(*),i},\omega_q,t_c)]$

}

}

}

}

ACKNOWLEDGMENT

This work was funded by the National Science Foundation under contract CCR-0073357. We thank Evan D. Morris for very informative discussions.

Send correspondence to Kevin J. Webb, School of Electrical and Computer Engineering, Purdue University, 465 Northwestern Avenue, West Lafayette, Indiana 47907-2035. E-mail, webb@purdue.edu; phone, 765-494-3373; fax, 765-494-2706.

REFERENCES

1. V. Ntziachristos, C. Bremer, and R. Weissleder, "Fluorescence imaging with near-infrared light," Eur. J. Radiol. **13**, 195–208 (2003).
2. J. S. Reynolds, T. L. Troy, R. H. Mayer, A. B. Thompson, D. J. Waters, K. K. Cornell, P. W. Snyder, and E. M. Sevick-Muraca, "Imaging of spontaneous canine mammary tumors using fluorescent contrast agents," Photochem. Photobiol. **70**, 87–94 (1999).
3. J. A. Reddy and P. S. Low, "Folate-mediated targeting of therapeutic and imaging agents to cancers," Crit. Rev. Ther. Drug Carrier Syst. **15**, 587–627 (1998).
4. U. Mahmood, C. Tung, J. A. Bogdanov, and R. Weissleder, "Near-infrared optical imaging of protease activity for tumor detection," Radiology **213**, 866–870 (1999).
5. A. Becker, C. Hessenius, K. Licha, B. Ebert, U. Sukowski, W. Semmler, B. Wiedenmann, and C. Grotzinger, "Receptor-targeted optical imaging of tumors with near-infrared fluorescent ligands," Nat. Biotechnol. **19**, 327–331 (2001).
6. J. E. Bugaj, S. Achilefu, R. B. Dorshow, and R. Rajagopalan, "Novel fluorescent contrast agents for optical imaging of *in vivo* tumors based on a receptor-targeted dye-peptide conjugate platform," J. Biomed. Opt. **6**, 122–133 (2001).
7. E. D. Morris, C. J. Endres, K. C. Schmidt, B. T. Christian, R. F. Muzic, Jr., and R. E. Fisher, "Kinetic Modeling in PET," in *Emission Tomography: the Fundamentals of PET and SPECT*, M. Wernick and J. Aarsvold, eds. (Academic, San Diego, Calif.,2004).
8. W. R. Potter, D. A. Bellnier, and T. J. Dougherty, "Optical methods for *in-vivo* pharmacokinetics," in *Optical Methods for Tumor Treatment and Detection: Mechanisms and Techniques in Photodynamic Therapy*, T. J. Dougherty, ed., Proc. SPIE 1645, 166–170 (1992).
9. R. A. Weersink, J. E. Hayward, K. R. Diamond, and M. S. Patterson, "Accuracy of noninvasive *in vivo* measurements of photosensitizer uptake based on a diffusion model of reflectance spectroscopy," Photochem. Photobiol. **66**, 326–335 (1997).
10. V. Ntziachristos, A. G. Yodh, M. Schnall, and B. Chance, "Concurrent MRI and diffuse optical tomography of breast after indocyanine green enhancement," Proc. Natl. Acad. Sci. U.S.A. **97**, 2767–2772 (2000).
11. M. Gurfinkel, A. B. Thompson, W. Ralston, T. L. Troy, A. L. Moore, T. A. Moore, J. D. Gust , D. Tatman, J. S. Reynolds, B. Muggenburg, K. Nikula, R. Pandey, R. H. Mayer, D. J. Hawrysz, and E. M. Sevick-Muraca,"Pharmacokinetics of ICG and HPPH-car for the detection of normal and tumor tissue using fluorescence, near-infrared reflectance imaging: a case study," Photochem. Photobiol. **72**, 94–102 (2000).
12. R. Springett, Y. Sakata, and D. T. Delpy, "Precise measurement of cerebral blood flow in newborn piglets from the bolus passage of indocyanine green," Phys. Med. Biol. **46**, 2209–2225 (2001).
13. D. J. Cuccia, F. Bevilacqua, A. J. Durkin, S. Merritt, B. J. Tromberg, G. Gulsen, H. Yu, J. Wang, and O. Nalcioglu, "*In vivo* quantification of optical contrast agent dynamics in rat tumors by use of diffuse optical spectroscopy with magnetic resonance imaging coregistration," Appl. Opt. **42**, 2940–2950 (2003).
14. S. R. Arridge, "Optical tomography in medical imaging," Inverse Probl. **15**, R41–R93 (1999).
15. A. B. Milstein, S. Oh, K. J. Webb, C. A. Bouman, Q. Zhang, D. A. Boas, and R. P. Millane, "Fluorescence optical diffusion tomography," Appl. Opt. **42**, 3081–3094 (2003).
16. M. S. Patterson and B. W. Pogue, "Mathematical model for time-resolved and frequency-domain fluorescence spectroscopy in biological tissues," Appl. Opt. **33**, 1963–1974 (1994).
17. E. M. Sevick-Muraca, G. Lopez, J. S. Reynolds, T. L. Troy, and C. L. Hutchinson, "Fluorescence and absorption contrast mechanisms for biomedical optical imaging using frequency-domain techniques," Photochem. Photobiol. **66**, 55–64 (1997).
18. S. Chandrasekhar, *Radiative Transfer* (Dover, New York, 1960).
19. C. H. Schmitz, H. L. Graber, H. Luo, I. Arif, J. Hira, Y. Pei, A. Bluestone, S. Zhong, R. Andronica, I. Soller, N. Ramirez, S.-L., S. Barbour, and R. L. Barbour, "Instrumentation and calibration protocol for imaging dynamic features in dense-scattering media by optical tomography," Appl. Opt. **39**, 6466–6486 (2000).
20. A. Y. Bluestone, G. Abdoulaev, C. H. Schmitz, R. L.

Barbour, and A. H. Hielscher, "Three-dimensional optical tomography of hemodynamics in the human head," Opt. Express **9**, 272–286 (2001).
21. V. Kolehmainen, S. Prince, S. R. Arridge, and J. P. Kaipio, "State-estimation approach to the nonstationary optical tomography problem," J. Opt. Soc. Am. A **20**, 876–889 (2003).
22. S. Prince, V. Kolehmainen, J. P. Kaipio, M. A. Franceschini, D. Boas, and S. R. Arridge, "Time-series estimation of biological factors in optical diffusion tomography," Phys. Med. Biol. **48**, 1491–1504 (2003).
23. U. Schmitt and A. K. Louis, "Efficient algorithms for the regularization of dynamic inverse problems: I. Theory," Inverse Probl. **18**, 645–658 (2002).
24. U. Schmitt, A. K. Louis, C. Wolters, and M. Vauhkonen, "Efficient algorithms for the regularization of dynamic inverse problems: II. Applications," Inverse Probl. **18**, 659–676 (2002).
25. Y. Zhang, A. Ghodrati, and D. H. Brooks, "Analysis of Spatial-Temporal Regularization Methods for Linear Inverse Problems from a Common Statistical Framework," in *Proceedings of the IEEE International Symposium on Biomedical Imaging: from Nano to Macro* (IEEE, 2004), Vol. **2**, pp. 772–775.
26. M. N. Wernick, E. J. Infusino, and M. Milosevic, "Fast spatio-temporal image reconstruction for dynamic PET," IEEE Trans. Med. Imaging **18**, 185–195 (1999).
27. T. E. Nichols, J. Qi, E. Asma, and R. M. Leahy, "Spatiotemporal Reconstruction of List-Mode PET Data," IEEE Trans. Med. Imaging **21**, 396–404 (2002).
28. B. W. Reutter, G. T. Gullberg, and R. H. Huesman, "Direct least-squares estimation of spatiotemporal distributions from dynamic SPECT projections using a spatial segmentation and temporal B-splines," IEEE Trans. Med. Imaging **19**, 434–450 (2000).
29. S. Ahn, J. A. Fessler, T. E. Nichols, and R. A. Koeppe, "Covariance of kinetic parameter estimators based on time activity curve reconstructions: preliminary study on 1-D dynamic imaging," in *Proceedings of the IEEE International Symposium on Biomedical Imaging: from Nano to Macro* (IEEE, 2004), Vol. **2**, pp. 368–371.
30. J. A. Jacquez, *Compartmental Analysis in Biology and Medicine* (The University of Michigan Press, Ann Arbor, Mich., 1985).
31. R. E. Carson and K. Lange, "The EM parametric image reconstruction algorithm," J. Am. Stat. Assoc. **80**, 20–22 (1985).
32. J. Matthews, D. Bailey, P. Price, and V. Cunningham, "The direct calculation of parametric images from dynamic PET data using maximum-likelihood iterative reconstruction", Phys. Med. Biol. **42**, 1155–1173 (1997).
33. M. Kamasak, C. A. Bouman, E. D. Morris, and K. Sauer, "Direct Reconstruction of Kinetic Parameter Images from Dynamic PET Data," in *Proceedings of the 37th Asilomar Conference on Signals, Systems and Computers* (IEEE Signal Processing Society, www.ieee.org/organizations/society/sp/conferences.html, 2003), pp. 1919–1923.
34. A. B. Milstein, J. J. Stott, S. Oh, D. A. Boas, R. P. Millane, C. A. Bouman, and K. J. Webb, "Fluorescence optical diffusion tomography using multiple-frequency data," J. Opt. Soc. Am. A **21**, 1035–1049 (2004).
35. A. B. Milstein, S. Oh, J. S. Reynolds, K. J. Webb, C. A. Bouman, and R. P. Millane, "Three-dimensional Bayesian optical diffusion tomography with experimental data," Opt. Lett. **27**, 95–97 (2002).
36. S. Oh, A. B. Milstein, R. P. Millane, C. A. Bouman, and K. J. Webb, "Source-detector calibration in three-dimensional Bayesian optical diffusion tomography," J. Opt. Soc. Am. A **19**, 1983–1993 (2002).
37. K. Sauer and C. A. Bouman, "A local update strategy for iterative reconstruction from projections," IEEE Trans. Signal Process. **41**, 534–548 (1993).
38. C. A. Bouman and K. Sauer, "A generalized Gaussian image model for edge-preserving MAP estimation," IEEE Trans. Image Process. **2**, 296–310 (1993).
39. J. J. Duderstadt and L. J. Hamilton, *Nuclear Reactor Analysis* (Wiley, New York, 1976).
40. J. S. Reynolds, C. A. Thompson, K. J. Webb, F. P. LaPlant, and D. Ben-Amotz, "Frequency domain modeling of reradiation in highly scattering media," Appl. Opt. **36**, 2252–2259 (1997).
41. J. C. Ye, K. J. Webb, C. A. Bouman, and R. P. Millane, "Optical diffusion tomography using iterative coordinate descent optimization in a Bayesian framework," J. Opt. Soc. Am. A **16**, 2400–2412 (1999).
42. J. C. Ye, C. A. Bouman, K. J. Webb, and R. P. Millane, "Nonlinear multigrid algorithms for Bayesian optical diffusion tomography," IEEE Trans. Image Process. **10**, 909–922 (2001).
43. A. Ishimaru, *Wave Propagation and Scattering in Random Media* (Academic, New York, 1978), Vol. 1.
44. F. Fedele, J. P. Laible, and M. J. Eppstein, "Coupled complex adjoint sensitivities for frequency-domain fluorescence tomography: theory and vectorized implementation," J. Chem. Phys. **187**, 597–619 (2003).
45. E. K. P. Chong and S. H. Zak, *An Introduction to Optimization* (Wiley, New York, 1996).
46. J. C. Adams, "MUDPACK: Multigrid portable FORTRAN software for the efficient solution of linear elliptic partial differential equations," Appl. Math. Comput. **34**, 113–146 (1989).
47. S. S. Saquib, C. A. Bouman, and K. Sauer, "ML parameter estimation for Markov random fields with applications to Bayesian tomography," IEEE Trans. Image Process. **7**, 1029–1044 (1998).
48. S. Oh, C. A. Bouman, and K. J. Webb, "A general framework for nonlinear multigrid inversion," IEEE Trans. Image Process. **14**, 125–140 (2005).
49. A. B. Milstein, M. D. Kennedy, P. S. Low, C. A. Bouman, and K. J. Webb, " Statistical approach for detection and localization of a fluorescing mouse tumor in Intralipid," Appl. Opt. **44**, 2300–2310 (2005).
50. R. B. Schulz, J. Ripoll, and V. Ntziachristos, "Experimental fluorescence tomography of tissues with noncontact measurements," IEEE Trans. Med. Imaging **23**, 492–500 (2004).